

LETTER TO THE EDITOR

# ALMA chemical survey of disk-outflow sources in Taurus (ALMA-DOT)

## II: Vertical stratification of CO, CS, CN, H<sub>2</sub>CO, and CH<sub>3</sub>OH in a Class I disk

L. Podio<sup>1</sup>, A. Garufi<sup>1</sup>, C. Codella<sup>1,2</sup>, D. Fedele<sup>1</sup>, E. Bianchi<sup>2</sup>, F. Bacciotti<sup>1</sup>, C. Ceccarelli<sup>2</sup>, C. Favre<sup>2</sup>, S. Mercimek<sup>1,4</sup>,  
K. Rygl<sup>3</sup>, and L. Testi<sup>5,6,1</sup>

<sup>1</sup> INAF - Osservatorio Astrofisico di Arcetri, Largo E. Fermi 5, 50125 Firenze, Italy  
e-mail: lpodio@arcetri.astro.it

<sup>2</sup> Univ. Grenoble Alpes, CNRS, IPAG, 38000 Grenoble, France

<sup>3</sup> INAF - Istituto di Radioastronomia & Italian ALMA Regional Centre, via P. Gobetti 101, 40129 Bologna, Italy

<sup>4</sup> Università degli Studi di Firenze, Dipartimento di Fisica e Astronomia, Via G. Sansone 1, 50019 Sesto Fiorentino, Italy

<sup>5</sup> European Southern Observatory, Karl-Schwarzschild-Strasse 2, 85748 Garching bei München, Germany

<sup>6</sup> Excellence Cluster Origins, Boltzmannstrasse 2, 85748 Garching bei München, Germany

Received -; accepted -

### ABSTRACT

The chemical composition of planets is inherited from that of the natal protoplanetary disk at the time of planet formation. Increasing observational evidence suggests that planet formation occurs in less than 1–2 Myr. This motivates the need for spatially resolved spectral observations of young Class I disks, as carried out by the ALMA chemical survey of Disk-Outflow sources in Taurus (ALMA-DOT). In the context of ALMA-DOT, we observe the edge-on disk around the Class I source IRAS 04302+2247 (the butterfly star) in the 1.3 mm continuum and five molecular lines. We report the first tentative detection of methanol (CH<sub>3</sub>OH) in a Class I disk and resolve, for the first time, the vertical structure of a disk with multiple molecular tracers. The bulk of the emission in the CO 2–1, CS 5–4, and o-H<sub>2</sub>CO 3<sub>1,2</sub>–2<sub>1,1</sub> lines originates from the warm molecular layer, with the line intensity peaking at increasing disk heights,  $z$ , for increasing radial distances,  $r$ . Molecular emission is vertically stratified, with CO observed at larger disk heights (aperture  $z/r \sim 0.41 - 0.45$ ) compared to both CS and H<sub>2</sub>CO, which are nearly cospatial ( $z/r \sim 0.21 - 0.28$ ). In the outer midplane, the line emission decreases due to molecular freeze-out onto dust grains (freeze-out layer) by a factor of  $> 100$  (CO) and 15 (CS). The H<sub>2</sub>CO emission decreases by a factor of only about 2, which is possibly due to H<sub>2</sub>CO formation on icy grains, followed by a nonthermal release into the gas phase. The inferred [CH<sub>3</sub>OH]/[H<sub>2</sub>CO] abundance ratio is 0.5–0.6, which is 1–2 orders of magnitude lower than for Class 0 hot corinos, and a factor  $\sim 2.5$  lower than the only other value inferred for a protoplanetary disk (in TW Hya, 1.3–1.7). Additionally, it is at the lower edge but still consistent with the values in comets. This may indicate that some chemical reprocessing occurs in disks before the formation of planets and comets.

**Key words.** Protoplanetary disks – Astrochemistry – ISM: molecules – Stars: individual: IRAS 04302+2247

### 1. Introduction

The chemical composition of exoplanets is determined by that of their natal environment, the protoplanetary disk. Recent studies suggest that planet formation occurs earlier than previously thought, that is, in disks of less than 1 Myr, which are massive enough to form planets with the observed exoplanetary masses (Tychoniec et al. 2020). Furthermore, these young disks show gaps in their dust grains distribution, which is a possible signature of forming planets (e.g., Fedele et al. 2018; Sheehan & Eisner 2017b, 2018). It is therefore crucial to probe the chemical composition of young disks around Class I sources ( $< 10^6$  years) in order to determine the following: what molecules are present in young disks and how they are distributed; whether disks inherit the chemical complexity observed at the protostellar stage (e.g., Lee et al. 2019a; Jørgensen et al. 2016) in terms of complex organic (COMs) and prebiotic molecules, as suggested by the recent work of Bianchi et al. (2019) and Drozdovskaya et al. (2019); and whether COMs are formed in the disk due to efficient ice chemistry in the cold midplane (e.g., Walsh et al. 2014).

According to thermo-chemical models, protoplanetary disks consist of three chemical layers (e.g., Aikawa et al. 2002; Dullemond et al. 2007; Dutrey et al. 2014, and references therein): (i) the hot surface layer, or disk atmosphere, where molecules are photodissociated; (ii) the warm molecular layer, where molecules are in the gas phase and gas-phase chemistry is at play; and (iii) the freeze-out layer, that is, the cold outer disk midplane where molecules freeze out onto dust grains. For each molecule, the freeze-out occurs at the disk radius and height where the dust temperature falls below the freeze-out temperature, which depends on the molecular binding energy. However, frozen-out molecules outside their snowline can be released into the gas via nonthermal desorption processes (e.g., Willacy & Woods 2009; Walsh et al. 2014; Loomis et al. 2015, and references therein). These processes are efficient in the molecular layer, that is, in the inner disk region and at increasing disk heights in the outer disk, due to (inter-)stellar UV and X-rays penetration. In contrast, molecules are only partially released into the gas phase in the outer midplane mostly due to reactive

and cosmic-ray-induced desorption (e.g., Walsh et al. 2014, and references therein). As a result, the chemical composition of the ices in the disk midplane remains largely hidden to observations. However, recent observations and modeling suggest that the relatively high gas-phase abundance and intensity of formaldehyde ( $\text{H}_2\text{CO}$ ) in the outer disk region can be explained by formation on, and a release from, the icy grains in the disk midplane (e.g., Carney et al. 2017; Kastner et al. 2018; Loomis et al. 2015; Öberg et al. 2017; Podio et al. 2019; Pegues et al. 2020, and references therein). A key molecule to test the chemical composition of ices in the midplane, where planets form, is methanol ( $\text{CH}_3\text{OH}$ ). This molecule is one of the building blocks for the formation of more complex organic molecules and, as opposed to formaldehyde,  $\text{CH}_3\text{OH}$  only forms on the icy mantles of dust grains (Watanabe & Kouchi 2002). According to disk models,  $\text{CH}_3\text{OH}$  can reach gas-phase abundances of up to  $10^{-8}$  (e.g., Walsh et al. 2014). However, due to its large partition function, to date, methanol has only been detected in the disks of TW Hya (Walsh et al. 2016) and of the young outbursting star V883 Ori (van 't Hoff et al. 2018; Lee et al. 2019b).

The most direct way to investigate the distribution and origin of molecules is to observe the vertical structure of disks so as to resolve the distinct chemical layers. The vast majority of the available resolved observations of molecular emission from protoplanetary disks, however, is relative to disks seen at low or medium inclinations ( $i < 75^\circ$ ). These observations only directly probe the disk radial structure, but not the vertical one. To date, resolved observations of edge-on disks have only been obtained in CO and its isotopologues (e.g., HH30 and IRAS 18059-3211, Louvet et al. 2018; Teague et al. 2020).

An ideal target to investigate the disk chemical structure is the edge-on disk ( $i = 90 \pm 3^\circ$ , Wolf et al. 2003) around the Class I source IRAS 04302+2247 (hereafter IRAS04302), also known as the butterfly star (Lucas & Roche 1997) and located in Taurus ( $d = 161 \pm 3$  pc, Galli et al. 2019). This source was observed with the IRAM-30m in CO,  $\text{H}_2\text{CO}$ , CS, SO,  $\text{HCO}^+$ , and HCN lines (Guilloteau et al. 2013, 2016), and with the PdBI in the continuum (Guilloteau et al. 2011). Based on their double-peaked profile,  $\text{H}_2\text{CO}$  and SO emission is attributed to the disk, while scattered-light images reveal the prominent outflow cavity (Lucas & Roche 1997; Padgett et al. 1999; Eisner et al. 2005). In this work, we report on new images of IRAS 04302 at  $\sim 0''.3$  ( $\sim 48$  au) taken with the Atacama Large Millimeter/submillimeter Array (ALMA) in the context of the ALMA-DOT program (ALMA chemical survey of Disk-Outflow sources in Taurus, see Garufi et al. 2020, and Garufi et al. in preparation).

## 2. Observations and data reduction

Observations were taken with ALMA-Band 6 on October 28, 2018 with baselines ranging from 15 m to 1.4 km (project 2018.1.01037.S, PI: L. Podio). The integration time sums up to  $\sim 113$  minutes. The bandpass and phase calibrators are J0423-0120 and J0510+1800, respectively. The correlator set-up consists of high-resolution (0.141 MHz) spectral windows (SPWs), covering CO 2-1, CN 2-1, o- $\text{H}_2\text{CO}$  3<sub>1,2</sub> - 2<sub>1,1</sub>, CS 5-4, and  $\text{CH}_3\text{OH}$  5<sub>0,5</sub> - 4<sub>0,4</sub> (A). The lines' properties are summarized in Table A.1. Data reduction was carried out using CASA 4.7.2. Self-calibration was performed on the continuum emission and applied on the line-free continuum and continuum-subtracted line emission. The signal-to-noise ratio (S/N) of the continuum

<sup>1</sup> A lower inclination,  $i \sim 76^\circ$  was estimated by Sheehan & Eisner (2017a)

improved by a factor of 3.4 after the self-calibration. The final maps were produced with `TCLEAN` by applying a manually selected mask on the visible signal. We used Briggs weighting with `robust=0.0` for the bright CO,  $\text{H}_2\text{CO}$ , CS, and CN lines to obtain high angular resolution maps, while we set Briggs weighting with `robust=2.0` for the faint  $\text{CH}_3\text{OH}$  line to maximize the S/N at the expense of angular resolution. The channel width is  $0.2 \text{ km s}^{-1}$ , except for the CS line ( $1.2 \text{ km s}^{-1}$ ), which is covered by the broad SPW for the continuum (1.129 MHz resolution). The clean beam of the self-calibrated maps ranges from  $0.31'' \times 0.26''$  to  $0.41'' \times 0.32''$  and the root mean square (r.m.s.) noise per channel is  $\approx 0.8 - 2.3 \text{ mJy beam}^{-1}$ . Moment 0 and 1 maps were produced over the velocity range  $[-1.2, +10] \text{ km s}^{-1}$ , except for CO ( $[-3, +14.2] \text{ km s}^{-1}$ ).

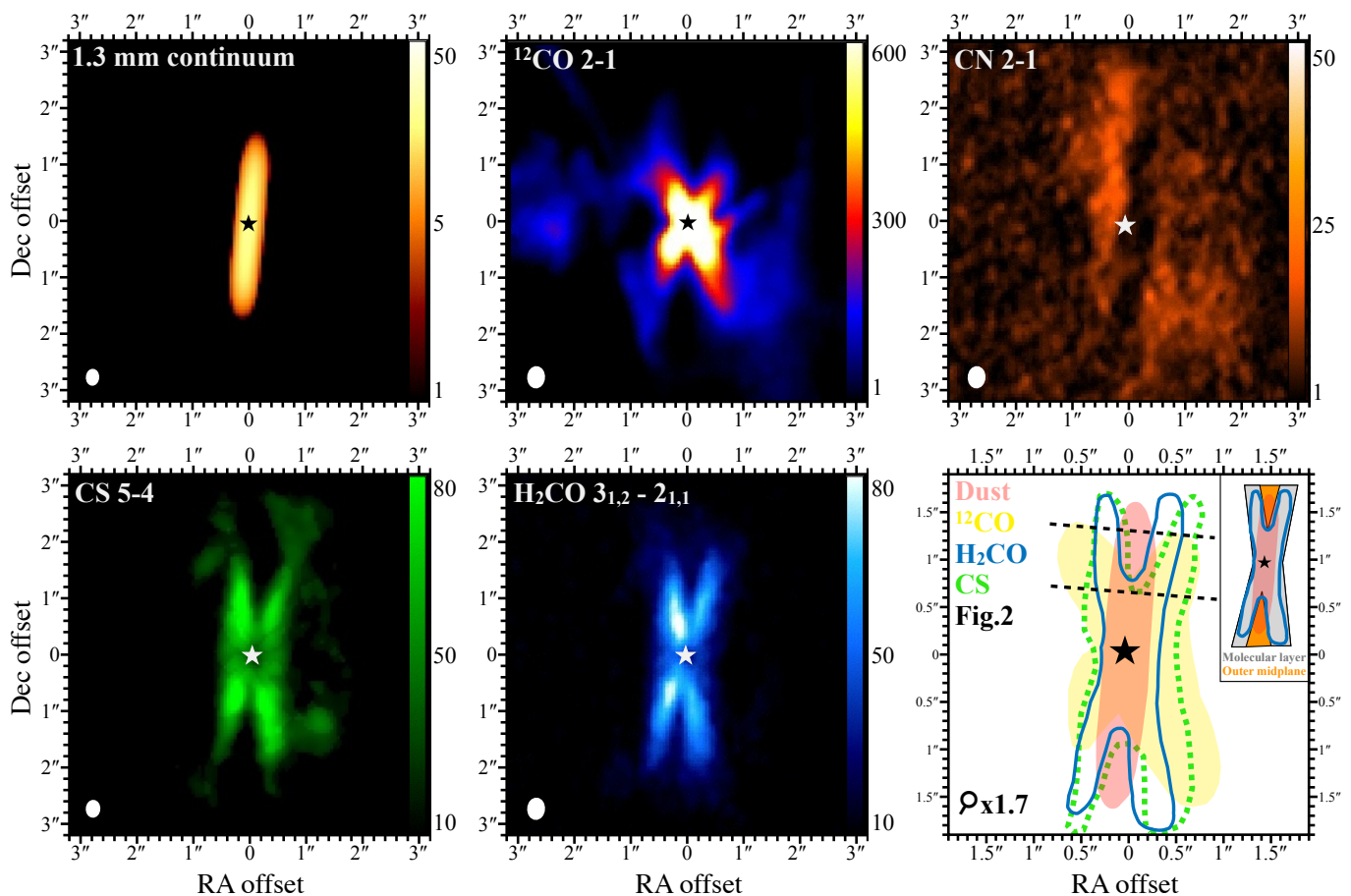
## 3. Results

Figure 1 shows the moment 0 maps of the continuum at 1.3 mm and molecular emission toward IRAS 04302, while moment 1 maps are shown in Fig. B.1. The continuum emission reveals the silhouette from the edge-on disk, which is roughly oriented along the north-south direction (P.A.= $175^\circ$ ). The half-width of the emission along the disk's minor axis is  $\sim 0.5''$ , which is more than twice the beam size along this direction ( $0.22''$ ). Thus, the disk's vertical extent is resolved. The distribution of the line emission is different across the various molecules both radially (i.e., across the disk radial extent) and vertically (i.e., across the disk height), as is discussed in the following sections.

### 3.1. Vertical distribution of molecular emission

The emission from CO 2-1, CS 5-4, and o- $\text{H}_2\text{CO}$  3<sub>1,2</sub> - 2<sub>1,1</sub> shows an X-shaped structure, that is, the line intensity peaks at increasing disk heights for increasing radial distances out to  $\sim 3''$  ( $\sim 480$  au). The CO emission is centrally-peaked, while the CS and  $\text{H}_2\text{CO}$  emission are dimmed in the inner  $0.3''$  ( $\sim 48$  au). As opposed to the other molecular tracers, the CN 2-1 emission does not show an X-shape and is instead detected at a constant height above the midplane across the disk's entire radial extent. Negative values are seen in the region corresponding to the 1.3 mm continuum emission, that is, the dusty disk is seen in silhouette. This is caused by continuum over-subtraction, which is likely due to the absorption of the continuum by interstellar and circumstellar CN molecules along the line of sight.

A vertical stratification of the CO, CS, and  $\text{H}_2\text{CO}$  emission across the disk height is observed, as summarized in the sketch shown in the bottom-right panel of Fig. 1. The CO emission extends up to larger disk heights than the other molecules. The  $\text{H}_2\text{CO}$  and CS emission is cospatial on the east side, while the CS emission is slightly higher on the west side. To quantify the disk height  $z$  from where the bulk of the emission in each molecule originates, we extracted the vertical profiles of the line intensity as a function of the radial distance. The profiles were extracted from the line moment 0 maps across the disk height, that is, perpendicularly to the disk's major axis by averaging the emission radially over three pixels ( $0''.18$ , corresponding to  $\sim 29$  au). The vertical profiles extracted to the north at radial distances of 115 and 230 au are shown in Fig. 2. The errors in the figure correspond to the standard deviation obtained over a nine-pixel box. We find that the disk height  $z$  where the emission peaks linearly increases with the radial distance  $r$ , resulting in a constant disk aperture  $z/r$  for each molecule. The emission in the different tracers is stratified, as  $z/r$  spans from 0.41-0.45 for CO to 0.22-0.28, and 0.21-0.25 for CS, and  $\text{H}_2\text{CO}$ , respectively. The



**Fig. 1.** Moment 0 maps of continuum at 1.3 mm and molecular emission toward IRAS 04302+2247. Molecular lines are the CO 2 – 1, CN 2 – 1, CS 5 – 4, and H<sub>2</sub>CO 3<sub>1,2</sub> – 2<sub>1,1</sub>. In each panel: The color wedge on the right shows the intensity in units of mJy beam<sup>-1</sup> and in logarithmic scale for the continuum, and in units of mJy beam<sup>-1</sup> km s<sup>-1</sup> and linear scale for the lines. The star in the center indicates the geometrical center of the continuum emission. The beam size is shown at the bottom left. The sketch in the bottom-right panel shows the comparison between the continuum (dust) and molecular emission, and it is zoomed in by a factor of 1.7. The black-dashed lines indicate the section over which the vertical profiles of Fig. 2 are obtained. The inset shows the regions named the molecular layer and outer midplane (see Sect. 3.3). North is up, east is left.

given  $z/r$  ranges include the scattering encountered along the four different disk surfaces, that is to say northeast, southeast, northwest, and southwest.

The molecular emission decreases in the outer disk midplane for  $r > 150$  au. The vertical profiles show that at a disk radius of 115 au, the intensity of all molecules is only slightly lower at the disk midplane with respect to their peak intensity (by a factor of 3 for CO, 2 for CS, and less than 2 for H<sub>2</sub>CO). At  $r = 230$  au instead, the emission in the midplane is lower with respect to the peak intensity by a factor of 2 for H<sub>2</sub>CO, and by a factor of 15 for CS. No CO emission is detected at the midplane, which means that it is lower than at the intensity peak by a factor of more than 100.

### 3.2. Tentative detection of methanol

The moment 0 map of the CH<sub>3</sub>OH 5<sub>0,5</sub>–4<sub>0,4</sub> (A) line shows emission up to 8 mJy beam<sup>-1</sup> km s<sup>-1</sup>. The emission does not show the same spatial distribution as any of the other tracers shown in Fig. 1, but it is confined within the H<sub>2</sub>CO emitting region, suggesting that it originates from the disk (see left panel of Fig. 3). This is further supported by the CH<sub>3</sub>OH spectral profile obtained by integrating over the H<sub>2</sub>CO emitting region (middle panel of Fig. 3). This reveals two peaks that are symmetrically displaced at  $\pm 2$  km s<sup>-1</sup> with respect to the systemic velocity ( $V_{\text{sys}} = +5.6$

km s<sup>-1</sup>), which is in perfect agreement with the peaks of H<sub>2</sub>CO (middle panel of Fig. 3). The CH<sub>3</sub>OH intensity obtained from the moment 0 map by integrating over the molecular layer, which is defined as the X-shaped region where CS and H<sub>2</sub>CO emission is brighter (area  $A = 4.3$  arcsec<sup>2</sup>, see sketch in Fig. 1), amounts to 42 mJy km s<sup>-1</sup>. The noise on the integrated emission<sup>2</sup> is 13 mJy km s<sup>-1</sup>; therefore, this is a  $3\sigma$  detection. As an a posteriori test, the integrated line intensity is consistent with the expectations for the [CH<sub>3</sub>OH]/[H<sub>2</sub>CO] abundance ratio (see Sect. 3.3).

### 3.3. Column densities in the midplane and molecular layer

The column densities of the detected molecular species were inferred by assuming local thermodynamic equilibrium and optically thin lines. The validity of these assumptions is discussed by Podio et al. (2019). The CS, H<sub>2</sub>CO, and CH<sub>3</sub>OH line intensities were integrated over the following two distinct regions: the disk molecular layer, as defined in Sect. 3.2 ( $A = 4.3$  arcsec<sup>2</sup>), and the outer disk mid-plane ( $A = 0.41$  arcsec<sup>2</sup>) (see sketch in Fig. 1). The noise on the integrated emissions,  $F_{\text{int}}$ , was derived just as for methanol<sup>2</sup>. If  $F_{\text{int}} < 3\sigma$ , we report the upper limit (Ta-

<sup>2</sup> The noise on the line integrated emission is  $\sigma_0 \times \sqrt{A/\theta_{\text{beam}}}$ , where  $\sigma_0$  is the r.m.s. of the moment 0 map,  $A$  is the area of integration, and  $\theta_{\text{beam}}$  is the beam size. The values of  $\sigma_0$  and  $\theta_{\text{beam}}$  are listed in Table A.1.

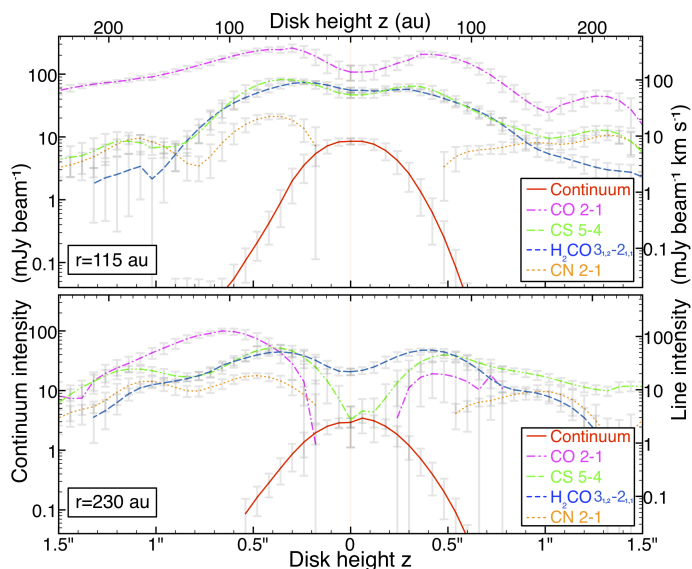


**Fig. 2.** Vertical intensity profiles of CO 2–1 (magenta), CS 5–4 (green), H<sub>2</sub>CO 3<sub>1,2</sub>–2<sub>1,1</sub> (blue) (in mJy beam<sup>−1</sup> km s<sup>−1</sup>), and of the 1.3 mm continuum (in mJy beam<sup>−1</sup>, red line). The vertical profiles were extracted at radial distances of 115 au (top) and 230 au (bottom).

ble 1). Then, the integrated line intensities were converted into column densities through the molecular parameters in Table A.1 (CDMS, Müller et al. 2005). As there are no estimates of the disk temperature, the excitation temperature is assumed to be 20–100 K in the molecular layer and 10–30 K in the outer midplane (see e.g., Walsh et al. 2010). The minimum and maximum column densities over this range of  $T_{\text{ex}}$  are summarized in Table 1. The assumed  $T_{\text{ex}}$  values are in agreement with those inferred from multi-line observations of CS and H<sub>2</sub>CO in a few Class II disks (e.g., Le Gal et al. 2019; Pegues et al. 2020), while no estimates of  $T_{\text{ex}}$  in Class I disks are available. The total H<sub>2</sub>CO and CH<sub>3</sub>OH column densities were derived assuming an ortho-to-para ratio of 1.8 – 2.8 (Guzmán et al. 2018) and the ratio of A-type to E-type forms to be one.

The average H<sub>2</sub>CO column density in the outer disk midplane is up to a factor of 8 lower than in the molecular layer, whereas the CS column density decreases by a factor of up to > 10 in the midplane, which is in agreement with the decrease in line intensity shown by the vertical profiles in Fig. 2. As for CH<sub>3</sub>OH, the column density is determined in the molecular layer, while only an upper limit is given for the outer midplane. From the inferred values, the abundance ratio between CH<sub>3</sub>OH and H<sub>2</sub>CO is  $\sim 0.5 - 0.6$  in the molecular layer and  $< 3.2$  in the midplane.

#### 4. Discussion

The observed molecular emission highlights the disk’s vertical stratification. The CO 2 – 1 emission probes an upper disk layer ( $z/r \sim 0.41 - 0.45$ ), which extends up to a larger disk height with respect to o-H<sub>2</sub>CO 3<sub>1,2</sub>–2<sub>1,1</sub> and CS 5–4 ( $z/r \sim 0.2 - 0.3$ ). The H<sub>2</sub>CO and CS emissions are roughly coincident and trace an intermediate disk layer. The analogous distribution of the two lines is explained by (i) the very similar upper level energy and critical densities ( $E_{\text{up}} = 33$  K, and 35 K, and  $n_{\text{cr}} \sim 7 - 5 \times 10^5$  cm<sup>−3</sup>, and  $17 - 9.5 \times 10^5$  cm<sup>−3</sup>, at 20 – 100 K, for the H<sub>2</sub>CO and the CS line, respectively, Shirley 2015) and (ii) the similar distribution of the H<sub>2</sub>CO and CS abundance in the disk suggested by thermo-chemical models (e.g., Fedele & Favre 2020).

**Table 1.** Integrated intensities and average column densities of CS, H<sub>2</sub>CO, and CH<sub>3</sub>OH calculated over the molecular layer ( $T_{\text{ex}} = 20 - 100$  K) and outer midplane ( $T_{\text{ex}} = 10 - 30$  K) (see Sect. 3.3).

Species	Disk region	$F_{\text{int}}$	$N$
		(mJy km/s)	(10 <sup>13</sup> cm <sup>−2</sup> )
CS	Molecular layer	2134 (31)	3.4–5.0
	Outer midplane	< 30	< 1.8, < 0.5
H <sub>2</sub> CO	Molecular layer	1865 (26)	7.2–25
	Outer midplane	72 (8)	2.8–5.6
CH <sub>3</sub> OH	Molecular layer	42 (13)	3.6–14.6
	Outer midplane	< 12	< 18

**Notes.** The integrated intensities (errors in brackets) refer to the CS 5 – 4, o-H<sub>2</sub>CO 3<sub>1,2</sub> – 2<sub>1,1</sub>, and CH<sub>3</sub>OH 5<sub>0,5</sub> – 4<sub>0,4</sub> (A) lines.

Both molecules are released from grains and/or formed in the gas phase in the molecular layer, following the photodissociation of CO, which makes available C for the formation of small hydrocarbons, together with atomic O. The CS is formed from reactions of small hydrocarbons with either ionized or atomic S (e.g., Le Gal et al. 2019), while the main formation route of H<sub>2</sub>CO is via the reaction CH<sub>3</sub>+O (e.g., Loomis et al. 2015). Additionally, CO 2 – 1 and CS 5 – 4 emissions strongly decrease in the outer disk-midplane, where molecules freeze-out onto dust grains (freeze-out layer). By contrast, H<sub>2</sub>CO is only a factor of 2 less intense, which indicates that the H<sub>2</sub>CO molecules trapped on the icy grains in the cold midplane are partially released by nonthermal processes (UV, X-ray, cosmic-rays-induced, and/or reactive desorption).

We tentatively detected CH<sub>3</sub>OH emission at  $3\sigma$  in the disk region where H<sub>2</sub>CO and CS emissions are bright, that is to say the warm molecular layer where molecules should be efficiently released from grains, while it remains undetected in the outer disk midplane. In the right panel of Fig. 3, the [CH<sub>3</sub>OH]/[H<sub>2</sub>CO] abundance ratio inferred for the Class I disk of IRAS 04302 is compared with the estimates obtained in hot corinos around Class 0 protostars, in the other Class I disks observed by ALMA-DOT, in the Class II disks of TW Hya and HD 163296, and in comets. The abundance ratio in the disk of IRAS 04302 ( $\sim 0.5 - 0.6$  for  $T_{\text{ex}} \sim 20 - 100$  K) is consistent with the upper limits derived for the other Class I and early Class II disks observed by ALMA-DOT (between  $< 0.7$  and  $< 3.2$ , Podio et al. 2019; Garufi et al. 2020, Garufi et al. in prep.). On the other hand, it is lower by a factor of  $\sim 2.5$  than that inferred for the Class II disk of TW Hya ( $\sim 1.27 - 1.73$  for  $T_{\text{ex}} \sim 25 - 75$  K, Walsh et al. 2016; Carney et al. 2019), while it is larger than the upper limit obtained for HD 163296 ( $< 0.24$ , Carney et al. 2019). As methanol forms on the dust grains due to CO freeze-out and subsequent hydrogenation, the lower [CH<sub>3</sub>OH]/[H<sub>2</sub>CO] in HD 163296 may be due to a smaller degree of CO ice chemistry in the warmer disks around Herbig stars (e.g., Pegues et al. 2020). The abundance ratios in Class I and Class II disks are from a factor of 2 to 2 orders of magnitude lower than the values inferred in the hot corinos around the Class 0 protostars IRAS 16293-2422 A and B in Taurus (Jørgensen et al. 2018; Persson et al. 2018; Manigand et al. 2020), and NGC1333-IRAS 4A and IRAS 2A in Perseus (Taquet et al. 2015). This difference may be due to an evolution of the methanol and formaldehyde abundance, which would indicate that the chemical processes occurring in the disk alter its chemical composition with respect to the protostellar stage (“disk reset” scenario). If instead the chemical composition of the ices in the disk is inher-

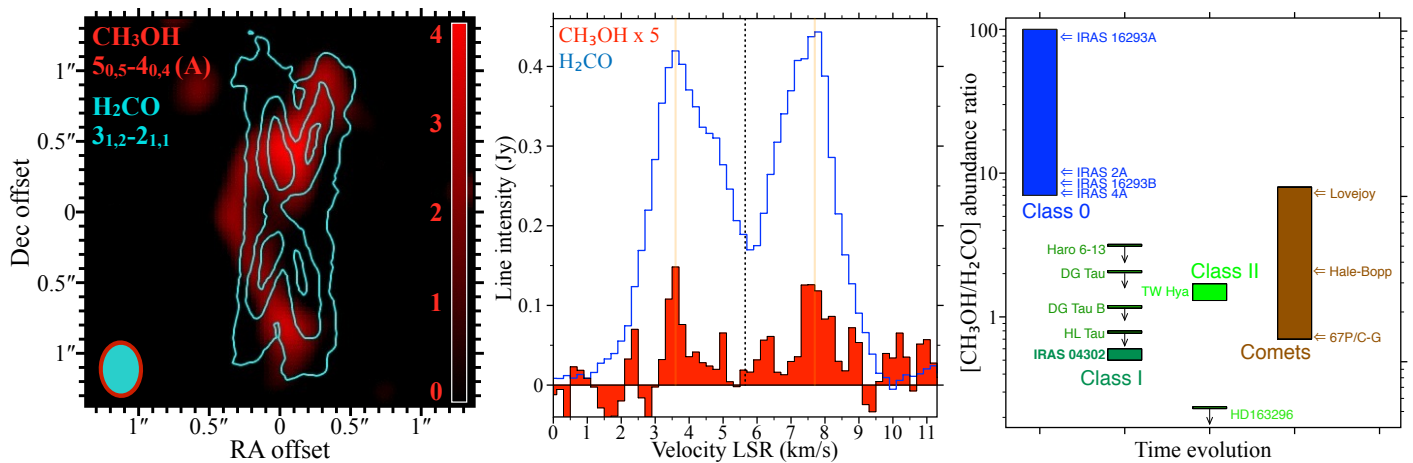


**Fig. 3.** *Left:*  $\text{CH}_3\text{OH } 5_{0,5}-4_{0,4}(\text{A})$  moment 0 map. The color wedge shows the intensity in units of  $\text{mJy beam}^{-1} \text{ km s}^{-1}$ . The cyan contours indicate the  $\text{H}_2\text{CO } 3_{1,2}-2_{1,1}$  emission of Fig. 1 at 20, 40, and 60  $\text{mJy beam}^{-1}$ . The beam sizes are shown at the bottom left with the relative colors. *Middle:* Spectral profiles of the  $\text{H}_2\text{CO}$  and  $\text{CH}_3\text{OH}$  lines integrated over the  $\text{H}_2\text{CO}$  emitting area. The  $\text{CH}_3\text{OH}$  profile is multiplied by 5. The solid-vertical lines indicate the peaks of the  $\text{H}_2\text{CO}$  profile and correspond to the peaks of the  $\text{CH}_3\text{OH}$  line. The dashed line indicates the source systemic velocity ( $V_{\text{sys}} = +5.6 \text{ km s}^{-1}$ ). *Right:*  $[\text{CH}_3\text{OH}]/[\text{H}_2\text{CO}]$  abundance ratio inferred for IRAS 04302 is compared with literature values inferred for Class 0 hot corinos, other Class I or early Class II disks observed by ALMA-DOT, Class II disks, and comets (references in the text).

ited from the protostellar stage and remains unaltered ("inheritance" scenario), the observed difference may either depend on the fact that the emission around Class 0 sources is unresolved or on the different processes which release the molecules in the gas phase. While, in the hot-corino, the ices are released in the gas phase by thermal desorption at  $T > 100 \text{ K}$  (e.g., Ceccarelli et al. 2007), in the disk midplane and molecular layer, non-thermal processes are at play (photo-desorption, cosmic-rays-induced, and/or reactive desorption, e.g., Walsh et al. 2014). A detailed comparison with thermo-chemical disk models is necessary to distinguish between the two competing scenarios. Finally, the  $[\text{CH}_3\text{OH}]/[\text{H}_2\text{CO}]$  abundance ratio in all disks except HD 163296 is comparable with the wide range found for comets 67P/C-G, Hale-Bopp, and Lovejoy ( $\sim 0.65-8$ , Biver et al. 2015; Rubin et al. 2019), even though IRAS 04302 sits at the lower limit of that range. The comparison in Fig. 3 suggests a change in the chemical composition in disks with respect to the protostellar stage, which is then inherited by forming planets and minor bodies, such as comets.

## 5. Conclusions

The nearly edge-on disk around the Class I source IRAS 04302 observed at  $\sim 48 \text{ au}$  resolution in the context of the ALMA-DOT campaign allows us to resolve, for the first time, the vertical structure of a protoplanetary disk in several molecular tracers. The CO, CS, and  $\text{H}_2\text{CO}$  maps probe the chemical stratification predicted by thermo-chemical models (e.g., Dutrey et al. 2014, and references therein): the warm molecular layer, with the height of the emitting region linearly increasing with the radial distance; and the freeze-out layer in the cold outer midplane where line emission decreases due to molecular freeze-out onto dust grains.

We report the first tentative detection of  $\text{CH}_3\text{OH}$  in the disk of a Class I source and constrain the abundance with respect to  $\text{H}_2\text{CO}$  to be 0.5–0.6. The inferred abundance ratio is 1–2 orders of magnitude lower than in hot corinos around Class 0 protostars, while it is only a factor of 2.5 lower than that estimated in the Class II disk of TW Hya and comparable with that inferred for comet 67P/C-G. This may be due to chemical evolution, that

is, to a chemical reset in the disk with respect to the protostellar stage and/or to the different processes responsible for the release of molecules in the gas phase (thermal desorption in hot corinos and nonthermal desorption in disks). A detailed modeling of the disk thermo-chemical structure is required to distinguish between inheritance and disk-reset scenarios.

*Acknowledgements.* We thank C. Spingola for the valuable help with the ALMA data reduction. This paper makes use of the ALMA data 2018.1.01037.S (PI L. Podio). ALMA is a partnership of ESO (representing its member states), NSF (USA) and NINS (Japan), together with NRC (Canada), MOST and ASIAA (Taiwan), and KASI (Republic of Korea), in cooperation with the Republic of Chile. This work was supported by: (i) the EU's Horizon 2020 research and innovation programme under Marie Skłodowska-Curie grant agreement No 811312 (Astro-Chemical Origins), and No 823823 (RISE DUST-BUSTERS); (ii) the ERC project "The Dawn of Organic Chemistry" (DOC), grant agreement No 741002; (iii) PRIN-INAF/2016 GENESIS-SKA; (iv) the Italian Ministero dell'Istruzione, Università e Ricerca through the grants Progetti Premiali 2012/iALMA (CUP-C52113000140001), 2017/FROTIERA (CUP-C61115000000001), and SIR-(RBS114ZRHR); (v) the Deutsche Forschungsgemeinschaft (DFG) - Ref no. FOR2634/1TE1024/1-1; (vi) the DFG cluster of excellence Origins (www.origins-cluster.de); (vii) the French National Research Agency in the framework of the Investissements d'Avenir program (ANR-15-IDEX-02), through the "Origin of Life" project of the Univ. Grenoble-Alpes.

## References

- Aikawa, Y., van Zadelhoff, G. J., van Dishoeck, E. F., & Herbst, E. 2002, *A&A*, 386, 622
- Bianchi, E., Codella, C., Ceccarelli, C., et al. 2019, *MNRAS*, 483, 1850
- Biver, N., Bockelée-Morvan, D., Moreno, R., et al. 2015, *Science Advances*, 1, 1500863
- Carney, M. T., Hogerheijde, M. R., Guzmán, V. V., et al. 2019, *A&A*, 623, A124
- Carney, M. T., Hogerheijde, M. R., Loomis, R. A., et al. 2017, *A&A*, 605, A21
- Ceccarelli, C., Caselli, P., Herbst, E., Tielens, A. G. G. M., & Caux, E. 2007, in *Protostars and Planets V*, ed. B. Reipurth, D. Jewitt, & K. Keil, 47
- Drozdovskaya, M. N., van Dishoeck, E. F., Rubin, M., Jørgensen, J. K., & Altwegg, K. 2019, *MNRAS*, 490, 50
- Dullemond, C. P., Hollenbach, D., Kamp, I., & D'Alessio, P. 2007, *Protostars and Planets V*, 555
- Dutrey, A., Semenov, D., Chapillon, E., et al. 2014, *Protostars and Planets VI*, 317
- Eisner, J. A., Hillenbrand, L. A., Carpenter, J. M., & Wolf, S. 2005, *ApJ*, 635, 396
- Fedele, D. & Favre, C. 2020, *A&A*, 638, A110
- Fedele, D., Tazzari, M., Booth, R., et al. 2018, *A&A*, 610, A24
- Galli, P. A. B., Loinard, L., Bouy, H., et al. 2019, *A&A*, 630, A137

- Garufi, A., Podio, L., Codella, C., et al. 2020, A&A, 636, A65
- Guilloteau, S., Di Folco, E., Dutrey, A., et al. 2013, A&A, 549, A92
- Guilloteau, S., Dutrey, A., Piétu, V., & Boehler, Y. 2011, A&A, 529, A105
- Guilloteau, S., Piétu, V., Chapillon, E., et al. 2016, A&A, 586, L1
- Guzmán, V. V., Öberg, K. I., Carpenter, J., et al. 2018, ApJ, 864, 170
- Jørgensen, J. K., Müller, H. S. P., Calcutt, H., et al. 2018, A&A, 620, A170
- Jørgensen, J. K., van der Wiel, M. H. D., Coutens, A., et al. 2016, A&A, 595, A117
- Kastner, J. H., Qi, C., Dickson-Vandervelde, D. A., et al. 2018, ApJ, 863, 106
- Le Gal, R., Öberg, K. I., Loomis, R. A., Pegues, J., & Bergner, J. B. 2019, ApJ, 876, 72
- Lee, C.-F., Codella, C., Li, Z.-Y., & Liu, S.-Y. 2019a, ApJ, 876, 63
- Lee, J.-E., Lee, S., Baek, G., et al. 2019b, Nature Astronomy, 3, 314
- Loomis, R. A., Cleeves, L. I., Öberg, K. I., Guzman, V. V., & Andrews, S. M. 2015, ApJ, 809, L25
- Louvet, F., Dougados, C., Cabrit, S., et al. 2018, A&A, 618, A120
- Lucas, P. W. & Roche, P. F. 1997, MNRAS, 286, 895
- Manigand, S., Jørgensen, J. K., Calcutt, H., et al. 2020, A&A, 635, A48
- Müller, H. S. P., Schlöder, F., Stutzki, J., & Winnewisser, G. 2005, Journal of Molecular Structure, 742, 215
- Öberg, K. I., Guzmán, V. V., Merchantz, C. J., et al. 2017, ApJ, 839, 43
- Padgett, D. L., Brandner, W., Stapelfeldt, K. R., et al. 1999, AJ, 117, 1490
- Pegues, J., Öberg, K. I., Bergner, J. B., et al. 2020, ApJ, 890, 142
- Persson, M. V., Jørgensen, J. K., Müller, H. S. P., et al. 2018, A&A, 610, A54
- Podio, L., Bacciotti, F., Fedele, D., et al. 2019, A&A, 623, L6
- Rubin, M., Altwegg, K., Balsiger, H., et al. 2019, MNRAS, 489, 594
- Sheehan, P. D. & Eisner, J. A. 2017a, ApJ, 851, 45
- Sheehan, P. D. & Eisner, J. A. 2017b, ApJ, 840, L12
- Sheehan, P. D. & Eisner, J. A. 2018, ApJ, 857, 18
- Shirley, Y. L. 2015, PASP, 127, 299
- Taquet, V., López-Sepulcre, A., Ceccarelli, C., et al. 2015, ApJ, 804, 81
- Teague, R., Jankovic, M. R., Haworth, T. J., Qi, C., & Ilee, J. D. 2020, MNRAS, 495, 451
- Tychoniec, Ł., Manara, C. F., Rosotti, G. P., et al. 2020, A&A, 640, A19
- van 't Hoff, M. L. R., Tobin, J. J., Trapman, L., et al. 2018, ApJ, 864, L23
- Walsh, C., Loomis, R. A., Öberg, K. I., et al. 2016, ApJ, 823, L10
- Walsh, C., Millar, T. J., & Nomura, H. 2010, ApJ, 722, 1607
- Walsh, C., Millar, T. J., Nomura, H., et al. 2014, A&A, 563, A33
- Watanabe, N. & Kouchi, A. 2002, ApJ, 571, L173
- Willacy, K. & Woods, P. M. 2009, ApJ, 703, 479
- Wolf, S., Padgett, D. L., & Stapelfeldt, K. R. 2003, ApJ, 588, 373

## Appendix A: Properties of the observed lines

In Table A.1, the properties of the observed lines (species, transition, frequency in MHz, upper level energy ( $E_{\text{up}}$ ) in K, and line strength ( $S_{ij}\mu^2$ ) in  $D^2$ ) and of the obtained line cubes and moment 0 maps (clean beam in  $''\times''$ , channel width in  $\text{km s}^{-1}$ , r.m.s noise per channel in  $\text{mJy beam}^{-1}$ , and r.m.s of the moment 0 map,  $\sigma_0$ , in  $\text{mJy beam}^{-1} \text{ km s}^{-1}$ ) are summarized.

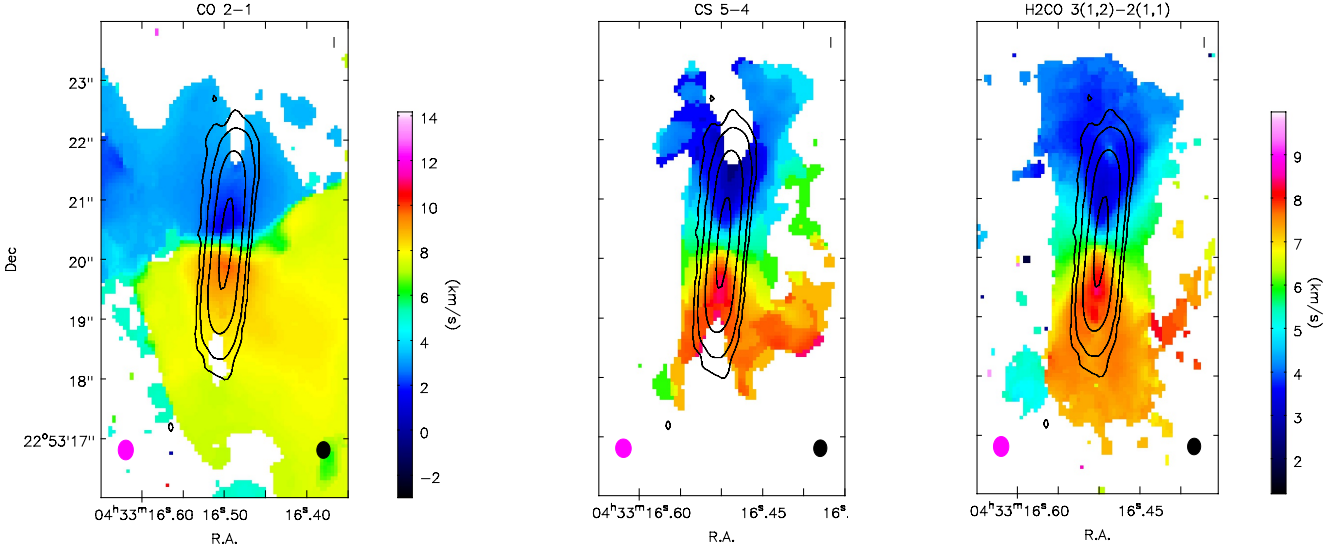
## Appendix B: Moment 1 maps of line emission

Figure B.1 shows the intensity weighted velocity distributions (moment 1 maps) of CO 2–1, CS 5–4, and o-H<sub>2</sub>CO 3<sub>1,2</sub>–2<sub>1,1</sub> obtained by applying a  $3\sigma$  clipping. The contours of the continuum emission at 1.3 mm are overplotted. The moment 1 maps show the typical disk rotation pattern. Even if the H<sub>2</sub>CO line intensity decreases in the inner 48 au and in the outer disk midplane (see the moment 0 map in Fig. 1 and vertical profiles in Fig. 2), the moment 1 map shows that the H<sub>2</sub>CO emission probes the gas rotation in the disk from the inner region out to a radius of  $\sim 3''$  ( $R_{\text{H}_2\text{CO}} \sim 480$  au). The H<sub>2</sub>CO emission is, therefore, more extended than the continuum by a factor of  $\sim 1.4$  ( $R_{\text{dust}} \sim 350$  au as determined from the  $3\sigma$  contour level). A similar velocity distribution is shown by CS 5–4 and CO 2–1, except that no emission at  $> 3\sigma$  is detected in the outer disk midplane, that is to say for radii  $\geq 1.4''$  corresponding to  $\sim 230$  au, as is also shown by the vertical profile at this radius (Fig. 2). Finally the moment 1 map of CO 2–1 also shows the velocity distribution of the gas in the envelope, as the emission in this line extends well beyond the gaseous disk structure probed by the o-H<sub>2</sub>CO 3<sub>1,2</sub>–2<sub>1,1</sub> line.

**Table A.1.** Properties of the observed lines from the CDMS database (Müller et al. 2005) and of the obtained line cubes and moment 0 maps.

Species	Transition	Frequency (MHz)	$E_{\text{up}}$ (K)	$S_{ij}\mu^2$ ( $\text{D}^2$ )	Clean beam ( $''\times''$ )	Channel width ( $\text{km s}^{-1}$ )	r.m.s. ( $\text{mJy beam}^{-1}$ )	$\sigma_0$ ( $\text{mJy beam}^{-1} \text{ km s}^{-1}$ )
CO	2 – 1	230538.000	17	0.02	0.33 $\times$ 0.25	0.2	2.3	9
CN <sup>(a)</sup>	2 – 1, J=5/2-3/2, F=5/2-3/2	226874.1908	16	4.2	0.34 $\times$ 0.26	0.2	2.0	4.1
	2 – 1, J=5/2-3/2, F=7/2-3/2	226874.7813	16	6.7				
	2 – 1, J=5/2-3/2, F=3/2-1/2	226875.8960	16	2.5				
CS	5 – 4	244935.557	35	19.1	0.31 $\times$ 0.26	1.2	0.8	4.6
<i>o</i> -H <sub>2</sub> CO	3 <sub>1,2</sub> – 2 <sub>1,1</sub>	225697.775	33	43.5	0.34 $\times$ 0.26	0.2	2.0	4.2
CH <sub>3</sub> OH-A	5 <sub>0,5</sub> – 4 <sub>0,4</sub>	241791.352	35	16.2	0.41 $\times$ 0.32	0.2	1.7	2.3

**Notes.** <sup>(a)</sup> The CN 2 – 1 transition consists of 19 hyperfine structure components. The ALMA SPW is centered on the second component listed in the table, which is the brightest hyperfine component of CN 2 – 1. Because of the line broadening due to disk kinematics, this is blended with the other two listed components.



**Fig. B.1.** Moment 1 maps of CO 2 – 1 (velocity scale from –3 to +14.2  $\text{km s}^{-1}$ ), CS 5 – 4, and H<sub>2</sub>CO 3<sub>1,2</sub> – 2<sub>1,1</sub> (velocity scale from +1.2 to +10  $\text{km s}^{-1}$ ). Black contours indicate the continuum emission at 1.3 mm ( $3\sigma$ ,  $10\sigma$ ,  $50\sigma$ , and  $200\sigma$  intensity levels, with  $\sigma = 0.05 \text{ mJy beam}^{-1}$ ). The magenta (black) ellipses on the bottom-left (right) corners show the line (continuum) beam.